AIAA JOURNAL
Vol. 34, No. 1, January 1996

Flowfield Surveys and Computations of a Crossing-Shock Wave/Boundary-Layer Interaction

T. J. Garrison*
Louisiana State University, Baton Rouge, Louisiana 70803
G. S. Settles†
Pennsylvania State University, University Park, Pennsylvania 16802
N. Narayanswami‡ and D. D. Knight§
Rutgers University, Piscataway, New Jersey 08903
and
C. C. Horstman¶
NASA Ames Research Center, Moffett Field, California 94035

A joint experimental and computational study has been performed to investigate the flowfield structure created by two crossing oblique shock waves interacting with a turbulent boundary layer. Such an interaction is of practical importance in the design of high-speed sidewall-compression inlets. The interaction is created by a test model, consisting of two sharp fins mounted at 15-deg angle of attack to a flat plate, placed in a Mach 3.85 freestream flow with a unit Reynolds number of 76 × 10^6/m. Two computational solutions, one using a Baldwin–Lomax algebraic turbulent eddy viscosity model and one using a modified κ–ε (Rodi) turbulence model, are compared with experimental flowfield data obtained from a fast-response five-hole probe. Both the experiment and the computations show that the flowfield is dominated by a large, low-Mach-number, low-total-pressure separated region located on the interaction centerline. A comparison of the results shows significant differences between experiment and computations within this separated region. Outside the separated region, the experiment and computations are in good agreement. Additionally, the comparison shows that both turbulence models provide similar results, with neither model being clearly superior in predicting the flowfield.

Introduction

SHOCK wave/boundary-layer interactions can arise in a variety of situations associated with high-speed flight vehicles. For example, such interactions occur at control surfaces, wing/fuselage junctions, and within many components of the propulsion system. One particular area of current interest is associated with the interactions created in a high-speed inlet. Within the inlet, the flowfield properties are strongly influenced by the nature of the shock wave/boundary-layer interactions which occur therein. Such interactions can produce complex shock wave patterns and large-scale flow separation, both of which significantly alter the inlet flow and subsequently affect the overall engine performance. Additionally, the large drag and heat transfer rates as well as fatigue loads due to interaction unsteadiness impose structural constraints on the inlet. Thus, an understanding of the shock wave/boundary-layer interactions within such inlets is paramount for effective inlet design.

One particular inlet configuration which has received a great deal of research attention in recent years is shown in Fig. 1a. This configuration simulates a generic high-speed sidewall-compression inlet, within which a pair of crossing oblique shock waves interacts with an incoming boundary layer. The flowfield created by this configuration, termed a crossing-shock interaction, has been studied both experimentally and computationally for a range of supersonic and hypersonic interactions. The majority of the experimental studies have focused on measurements made on the model surface,[1–7] with only a limited amount of data being available within the outer flowfield.[8–15] The data from these experiments have been used to understand the crossing-shock flow and to assess several computed solutions of the flowfield.[16–22] Although these experimental and computational efforts have shed a great deal of light on the structure of the crossing-shock interaction, the lack of experimental flowfield data has restricted the understanding of the outer flow as well as limited the evaluation of the computed solutions.

To address the need for additional flowfield data, five-hole probe measurements were recently made for a supersonic crossing-shock interaction. The goals of this paper are to describe the results of those measurements and to compare the experimental data with two computational solutions using different turbulence models. The results provide significant additional insight into the interaction physics as well as highlight the capabilities of current computational fluid dynamics models to predict a complex flow such as the crossing-shock interaction.

Description of Experiments

Wind-Tunnel Facility and Test Conditions

The experiments were performed in the Pennsylvania State Gas Dynamics Laboratory's Supersonic Wind Tunnel Facility, which is an intermittent blowdown tunnel with a test section size of 15 × 17 × 60 cm. The experiments described in this paper were carried out at a Mach number of 3.85, with a stagnation pressure of 1500 kPa, a stagnation temperature of 295 K, and a unit Reynolds number of 76 × 10^6 /m. Typical run times of 45 s were achieved at these conditions.

Test Model

Figure 1 shows the model geometry used for the crossing-shock experiments. This model consists of two vertical fins, both at angle of attack α, mounted on a horizontal flat plate. The flat plate generates an equilibrium, nearly adiabatic, zero-pressure-gradient

Presented as Paper 94-2273 at the AIAA 25th Fluid Dynamics Conference, Colorado Springs, CO, June 20–23, 1994; received July 6, 1994; revision received March 13, 1995; accepted for publication March 17, 1995. Copyright © 1994 by the authors. Published by the American Institute of Aeronautics and Astronautics, Inc., with permission.

*Assistant Professor, Mechanical Engineering. Member AIAA.
†Professor, Mechanical Engineering and Director, Gas Dynamics Laboratory. Associate Fellow AIAA.
‡Research Staff; currently Staff Engineer, FSI International, Chaska, MN 55318. Member AIAA.
§Professor, Mechanical and Aerospace Engineering. Associate Fellow AIAA.
¶Senior Scientist, Fluid Dynamics Division. Associate Fellow AIAA.

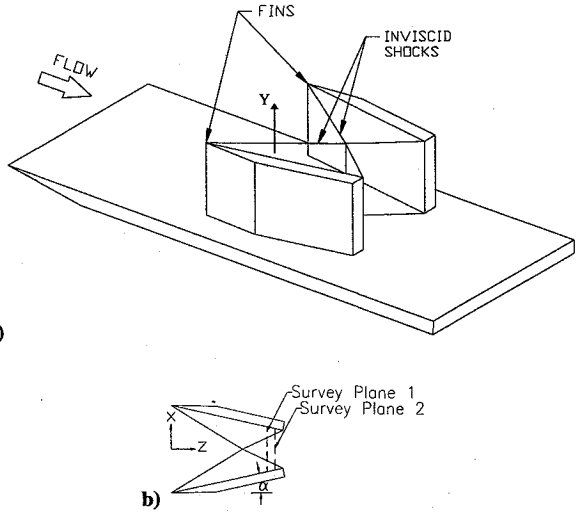

Fig. 1 Experimental crossing-shock model: a) perspective view and b) top view.

turbulent boundary layer which interacts with the two crossing oblique shock waves generated by the fins. The incoming properties of the boundary layer at the fin leading-edge location are $\delta = 3.5$ mm, $\delta^* = 1.12$ mm, and $\theta = 0.13$ mm. Further details are reported in Ref. 14.

The fins are located 21.3 cm downstream of the plate leading edge, with a transverse distance between the fin leading edges of 9.75 cm. The height of the fins is 8.25 cm, a value large enough to be effectively "semi-infinite." For the measurements described herein, both fins were positioned at 15-deg angle of attack, producing a symmetric interaction about the plane $X = 0$.

Five-Hole Probe Surveys

Flowfield surveys within the crossing-shock interaction were made using a recently developed fast-response five-hole probe. The probe tip, which is 1 mm in diameter, contains five 0.18-mm i.d. stainless-steel tubes. Because of the close spacing between the five orifices, the probe has excellent spatial resolution and can accurately make measurements in flows with large spatial gradients. The details of the probe design and calibration are given by Naughton et al.[23] and Naughton.[24] The outputs of the five-hole probe are the local Mach number M, pitot pressure P_p, pitch and yaw angles ϕ and ψ, respectively, and the static and stagnation pressures P and P_t, respectively. The probe is designed to measure Mach number over the range from 1.5 to 4.0. Based on a detailed calibration of the probe, measurement uncertainties are ±4% for Mach number, ±8% for the stagnation, pitot, and static pressures, and ±2 deg for the flow angles.[23]

The probe surveys of the crossing-shock interaction were performed at two Z planes, identified in Fig. 1b, located 113 and 123 mm downstream of the fin leading edges. At each of the survey planes an array of measurements was taken on an equally spaced grid with 1-mm increments in both the X and Y directions. Because of the symmetry of the crossing-shock interaction, only half of the interaction was surveyed at each Z plane. (The symmetry of the interaction was first verified through a limited set of surveys made on either side of the plane of symmetry.)

Description of Computations

Both computations described in this paper solve the full three-dimensional mean compressible Reynolds-averaged Navier–Stokes equations in strong conservation form (see, e.g., Ref. 25). The main difference between the two computations lies in the turbulence model used. The computation by Narayanswami and Knight models turbulence through the Baldwin–Lomax[26] (B–L) algebraic eddy-viscosity model. The numerical algorithm employed in this computation is the hybrid explicit-implicit scheme of Knight.[27] The computation by Horstman uses a modified κ–ε turbulence model[28] along with the hybrid numerical scheme of MacCormack.[29]

In both solutions, the computational geometry is set to match that of the experiment. Because of the symmetry of the crossing-shock interaction, however, the computations solve only half of the experimental domain. The grid size for the B–L computation is $66 \times 66 \times 44$ in the X, Y, and Z directions, respectively, whereas the grid size of the κ–ε computation is $40 \times 64 \times 79$. These grid sizes were selected based on previous grid resolution studies performed for three-dimensional shock wave/turbulent boundary-layer interactions at Mach 3 and Mach 8.3 (Refs. 19 and 30). The grids had variable spacing in all three directions, with grid points clustered near the model surfaces and in the region of the inviscid shock intersection. Further details on the grid spacing and computational geometry are given in Ref. 9.

The boundary conditions for both computations are as follows. 1) On the inflow boundary, an incoming two-dimensional equilibrium turbulent boundary-layer profile is prescribed to match the experiment. 2) On both the fin and plate surfaces, the velocity vector and normal gradient of static pressure, $\partial P/\partial n$, are set to zero. The wall temperature is set to $1.06\ T_{aw}$, to match the experiment. 3) On the plane of symmetry, the normal component of velocity is set to zero, as are the normal gradients of static pressure, temperature, and the remaining two velocity components. 4) On the top and outflow boundaries, the gradient of all flow variables is set to zero. Both computations were performed on a Cray Y-MP (single processor) and each required over 30 h of CPU time.

Results

Overall Flowfield

Because the basic features of the flowfield do not change significantly between the two survey planes shown in Fig. 1b, the following discussion will focus on results for the most upstream plane only ($Z = 113$ mm). Additionally, to facilitate the description of the five-hole probe results, it is useful to first review the structure of the crossing-shock interaction as determined from previously performed flow visualizations.[9,14] Figure 2 shows a model of the flowfield taken from Ref. 14, depicting the main flowfield features within the plane $Z = 113$ mm (the same plane surveyed with the five-hole probe). This model was extracted from a complete flowfield visualization and reveals the various shock waves, sliplines, and separated flow region within the plane of interest. Because of the symmetry of the crossing-shock interaction, the schematic of Fig. 2 only shows the flowfield features to the right of the symmetry plane (labeled S). The terminology used in Fig. 2 is consistent with that of Ref. 9.

The main features of interest within the flowfield model are the large separated flow region on the interaction centerline and the complex overlying shock structure. Within the separated region, two counter-rotating vortices are known to reside, with the approximate configuration of the vortex to the right of the symmetry plane identified in Fig. 2. The intent of the remaining discussion is to supplement this semiquantitative model with the detailed five-hole probe data and to compare the results with the two computed solutions. For more detailed information on the complete flowfield model the interested reader should consult Refs. 9 and 14.

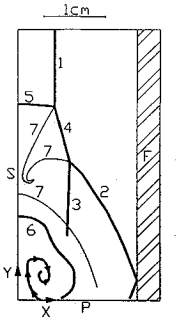

Fig. 2 Flowfield model at Z = 113 mm: P, plate; F, fin; S, symmetry plane; 1, reflected inviscid shock; 2, reflected separation shock; 3, reflected rear shock; 4, bridge shock; 5, centerline shock; 6, separated flow region; 7, sliplines.

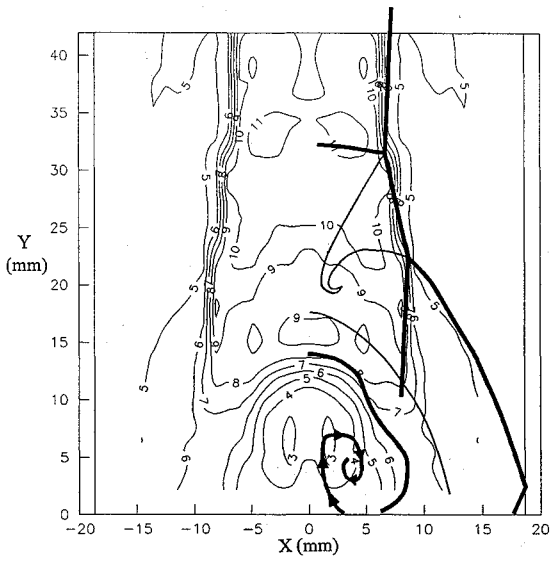

Fig. 3 Comparison of the experimental static pressure contours P/P_∞ with the flowfield model of Fig. 2.

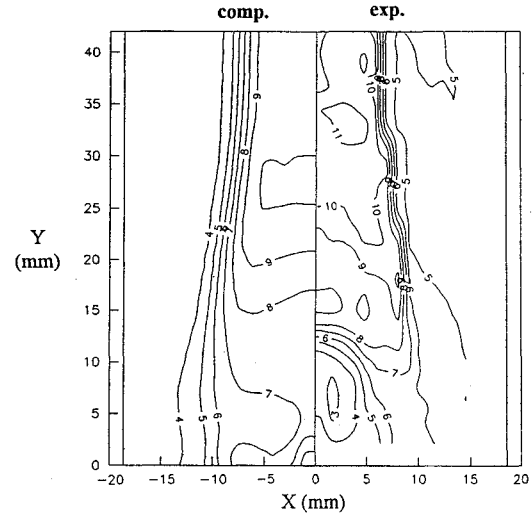

Fig. 4 Comparison of the static pressure P/P_∞ predicted by the B–L computation.

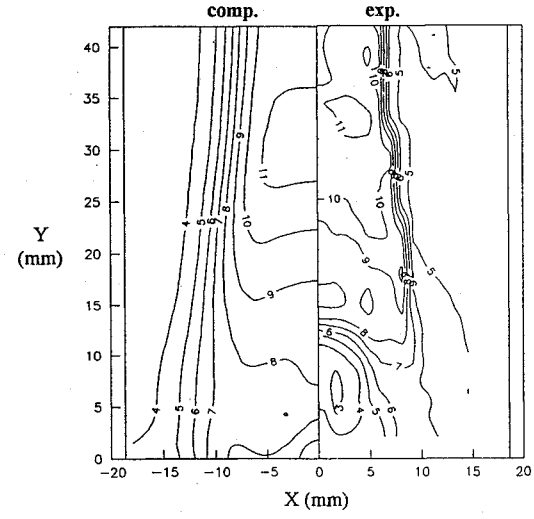

Fig. 5 Comparison of the static pressure P/P_∞ predicted by the κ–ε computation.

Static Pressure

Figure 3 shows the normalized static pressure contours, P/P_∞, obtained from the experimental five-hole probe surveys. Because the static pressure is sensitive even to weak oblique waves, such contours reveal most of the flowfield features. Overlaid on Fig. 3 is the corresponding flowfield diagram extracted from the planar laser scattering (PLS) visualizations (i.e., Fig. 2). From Fig. 3, it can be seen that the static pressure contours compare quite well with the shock structure taken from the PLS images. In this figure, the reflected separation, rear, and inviscid shocks, along with the "bridge" shock, are easily identified. The shock segment labeled the centerline shock in Fig. 2 does not clearly appear in the experimental pressure contours of Fig. 3, but can be verified by plotting the static pressure along discrete vertical cuts. The sliplines are not expected to appear, since they are streamlines across which a static pressure jump cannot occur.

In addition to locating shock waves, the static pressure contours can be used to gauge the strength of the various waves. From Fig. 3, it can be seen that the reflected separation shock is relatively weak, inducing only a slight static pressure rise. In contrast, the reflected rear shock is much stronger, with a pressure rise across it comparable to that across the reflected inviscid shock. Similarly, the bridge shock is comparable in strength to the reflected inviscid shock, whereas the centerline shock is very weak.

Figures 4 and 5 provide a comparison between the experimental normalized static pressure contours and those predicted by the B–L and κ–ε computations, respectively. In these figures, data for $X > 0$ are experimental whereas data for $X < 0$ are computational. It is possible to compare the results in this manner because of the symmetry of the crossing-shock interaction. It should also be noted that the contour increment is the same for both experiment and computation.

There are several important observations that can be made from Figs. 4 and 5. Considering the separated flow region first, there are significant differences between the computations and experiment within this region. The experimental contours show that the static pressure decreases significantly toward the center of this region whereas the computations predict a nearly uniform static pressure distribution. Additionally, in the experiment, the static pressure contours clearly delineate the size and shape of the separated region, but its presence is indiscernible in both computations. As shown in the following section, however, the separated region is apparent in the computed pitot pressure. Thus, the separated region is present in the computations but just not revealed by the static pressure. This is discussed further in the following section.

It is also clear from these figures that the computations are unable to precisely capture the shock waves within the flowfield. Even the pressure rise of the reflected inviscid shock, a strong wave that is unaffected by the underlying viscous effects, is spread over a significant distance. This is especially true for the κ–ε computation. The smearing of the shock waves by the computations is significantly greater than that by the five-hole probe and is orders of magnitude greater than that of the PLS images shown in Refs. 8, 9, and 14. The smearing of the computed shock waves is primarily due to the local coarseness of the grid, with the shocks typically spread over about three grid points. Referring to Fig. 2, a majority of the waves within the interaction, such as the reflected separation and rear shocks, and the bridge shock, cannot easily be distinguished as separate, distinct waves within the computations.

The contour plots shown in Figs. 4 and 5 provide a means to compare data over the entire plane. From these plots, however, it is somewhat difficult to quantitatively assess the degree to which the experiment and computations differ. For this purpose, it is more useful to compare the experiment and computations along discrete lines or "cuts." This is done in Fig. 6, which shows the static pressure variation in the Y direction at two X locations, namely, $X = 0$ and $X = 5$ mm. Figure 6a shows the normalized static pressure variation along the symmetry plane ($X = 0$). From this figure, it is clear that within the separated region ($Y < \approx 12$ mm) the computations significantly overpredict the static pressure by as much as a factor of 2.5. Above the separated region, where the flow is essentially inviscid, the computations and experiment are in good agreement. Overall, the pressure variation along the symmetry plane predicted by the B–L model is in slightly better agreement with the experiment than that predicted by the κ–ε model.

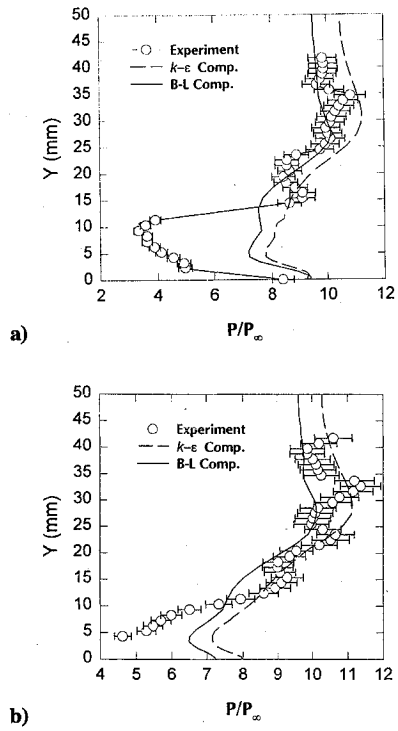

Fig. 6 Comparison of static pressure variation in the Y direction at a) $X = 0$ mm and b) $X = 5$ mm.

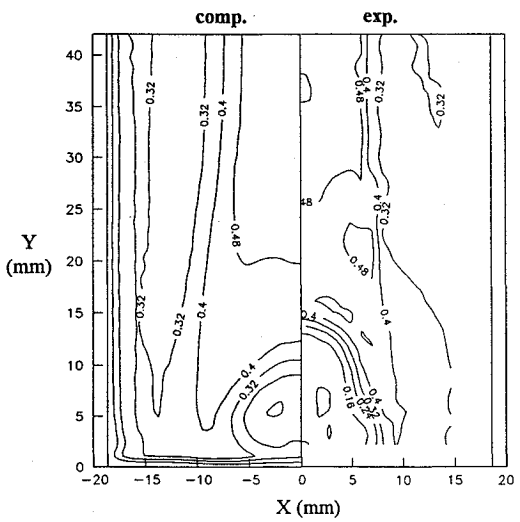

Fig. 7 Comparison of the pitot pressure $P_p/P_{t\infty}$ predicted by the B–L computation.

Along the cut at $X = 5$ mm, Fig. 6b, which passes along the outside edge of the separated region, similar conclusions can be drawn. However, the errors near $Y = 0$ are not as large as those in Fig. 6a. Comparing Figs. 4–6, it can be seen that the computational results are similar and that neither computation can be identified as being superior.

Pitot Pressure

Figures 7 and 8 compare the experimental normalized pitot pressure contours, $P_p/P_{t\infty}$, to those predicted by the B–L and κ–ε computations, respectively. As with the static pressure contours, the computed pitot pressure contours do not clearly resolve the individual waves within the interaction. Unlike the static pressure contours, however, both sets of computed pitot pressure contours do show the separated flow region. The vertical extent of the separated region is smaller in both computations than that observed experimentally.

The fact that the computed pitot pressure reveals the presence of the separated region suggests that the computations capture an essential aspect of the flow; the low-energy incoming boundary layer

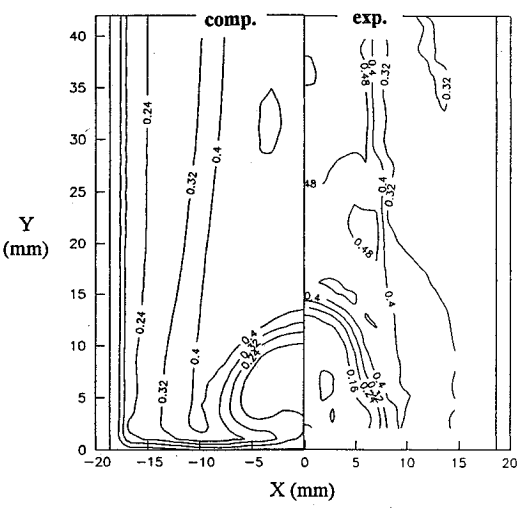

Fig. 8 Comparison of the pitot pressure $P_p/P_{t\infty}$ predicted by the κ–ε computation.

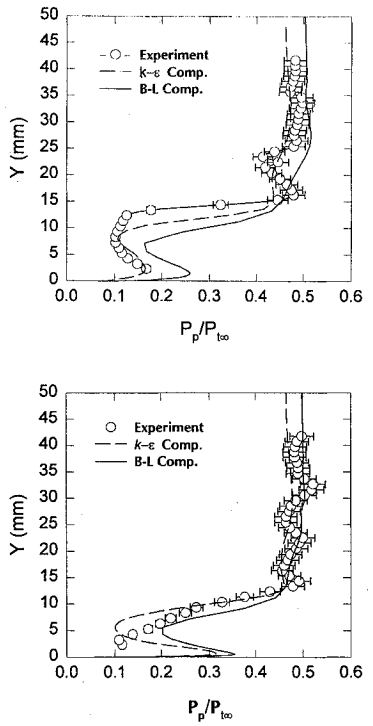

Fig. 9 Comparison of pitot pressure variation in the Y direction at a) $X = 0$ mm and b) $X = 5$ mm.

fluid separates from the plate and accumulates near the model centerline. It also appears that the computed static pressure imposed on this viscous region by the outer flowfield is not accurately predicted, however, suggesting problems in the computed wave structure.

Similarly to Fig. 6, Fig. 9 shows the pitot pressure variation for two vertical cuts at $X = 0$ and $X = 5$ mm. For the plot along the symmetry plane (Fig. 9a), except for slightly underpredicting the vertical extent of the separated region, the κ–ε computation accurately predicts the pitot pressure. The results of B–L computation are only slightly inferior to those of the κ–ε. For the plot along $X = 5$ mm (Fig. 9b), except for $5 < y < 10$ mm, the κ–ε computation is in very close agreement with the experiment over the entire range.

Stagnation Pressure

Figure 10 shows the experimental stagnation pressure contours, $P_t/P_{t\infty}$. This figure shows that, outside the separated region, the inlet type crossing-shock interaction produces an essentially uniform total pressure flow, recovering approximately 65% of the freestream stagnation pressure. Within the separated zone, however, the stagnation pressure recovery is less than 20%. This large bulbous separated

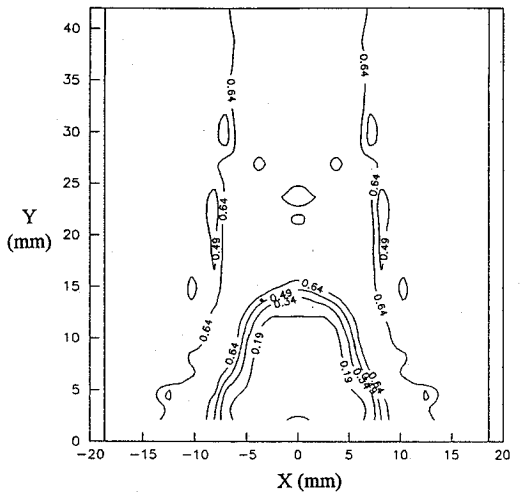

Fig. 10 Experimental total pressure contours $P_t/P_{t\infty}$.

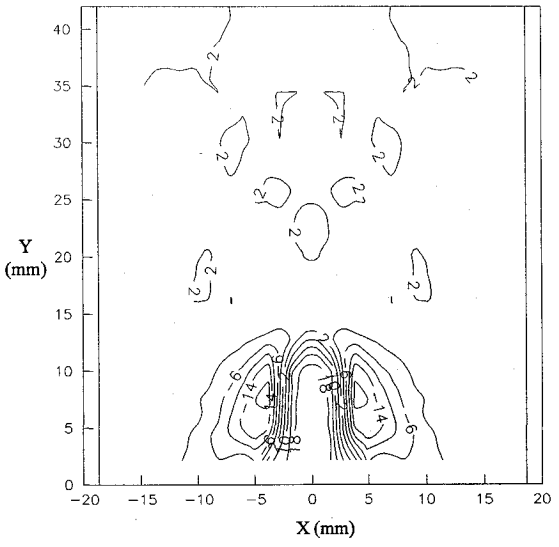

Fig. 11 Experimental pitch angle contours.

region, extending a significant distance away from the wall, is clearly a detriment to high-speed inlet performance.

A comparison with the computed total pressure contours (not shown) exhibits similar results to those of the pitot pressure. The κ–ε computation closely matches the experiment whereas the B–L computation slightly overestimates the recovery within the separated region and underestimates the size of the region.

Mach Number

Results of the experimental Mach number measurements (not shown) reveal the large separated region on the interaction centerline is comprised of low-Mach-number fluid. As with the other flowfield properties, within the separated region, both computations fail to accurately predict the Mach number. Outside of the separated region, however, both computations are within the experimental uncertainty.

Flow Angles

Figure 11 gives the experimental contours of the pitch angle, defined as $\phi = \tan^{-1}[M_y/\sqrt{M_x^2 + M_z^2}]$. The pitch angle represents the flow angle in the Y–Z plane, taken as positive for deflections in the positive Y direction (upward from the flat plate). From this figure, it can be seen that, outside of the separated region, there is little pitch in the flow.

Within the separated region, these contours show that near the centerline there is a significant vertical deflection away from the plate surface. Here, pitch angles as large as 18 deg are present. Away from the centerline, the flow is deflected downward, toward the plate, as shown by the regions with negative pitch angles. The

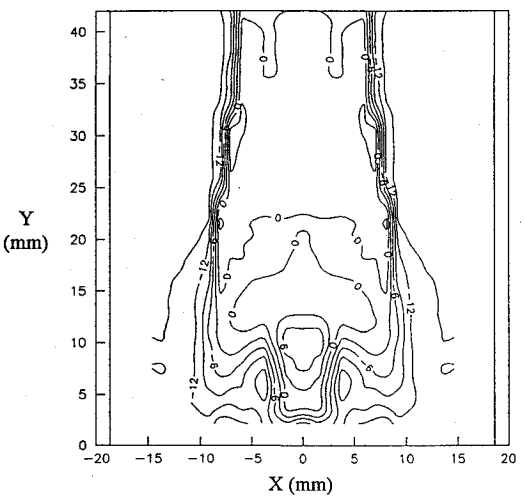

Fig. 12 Experimental yaw angle contours.

observed results are consistent with the known presence of two large, counter-rotating vortices located within the separated region, as sketched in Fig. 2.

Based on these results, it seems clear that the two counter-rotating vortices (remnants of the separation vortices of the two original single-fin interactions) located inside the separated region pull fluid from near the plate surface upward, along the interaction centerplane. As the fluid is pushed farther into the outer flow, it is turned away from the centerplane and deflected back toward the plate. Within the center of the separated region, it is observed that the vertical component of the Mach number, M_y, is 0.5. Compared to a total Mach number of approximately 1.5, this shows that a significant fraction of the total Mach number in the separated region is associated with the Y component.

The corresponding experimental yaw angle contours, where the yaw angle is defined as $\Psi = \tan^{-1}(M_x/M_z)$, are shown in Fig. 12. The yaw angle specifies the flow angle in the X–Z plane and is taken as negative for deflections toward the centerline (i.e., toward $X = 0$). The yaw contours clearly show the reflected inviscid shocks, across which there are large yaw angle variations. Between the reflected inviscid shock and the fin, the yaw angle is 15 deg, whereas in the region between the reflected inviscid shocks, the yaw angle is zero. This is as predicted from inviscid theory and is required to satisfy continuity. The yaw angles also show behavior indicative of the reflected separation and rear shocks as well as the bridge shock. The influence of the centerline shock does not appear, since it is horizontally oriented.

It should be noted that the contouring routine used here produces an anomaly in the yaw contours in which nonzero contour lines cross the centerplane. Clearly, the symmetry of the crossing-shock interaction requires that the yaw angle be zero everywhere on the plane of symmetry. On either side of the centerplane, however, the yaw angles may be nonzero. In instances where nonzero yaw angles occur close to the centerline, the contour package erroneously connects these points across the centerline. Thus, this artifact must be ignored in interpreting the resulting contours.

Inside the separated region, near the plate surface, the yaw angles are negative, indicating that the flow is being directed toward the centerplane. Near the top of the separated region, in the vicinity of the centerplane, the flow is directed away from the centerplane. At the top of the separated region and slightly further from the centerplane, however, the yaw angle becomes negative and the flow is once again directed toward the centerline.

By combining these observations with the previously described pitch angle results, the flowfield structure within the separated region can be determined. The result is the mushroom-shaped vortical flow pattern earlier depicted within the separated region of Fig. 2. It should be noted that Fig. 2 illustrates the flow pattern within a crossflow plane. From a three-dimensional standpoint, the additional axial velocity component causes the fluid particles within the separated region to undergo a spiraling motion. Further details of

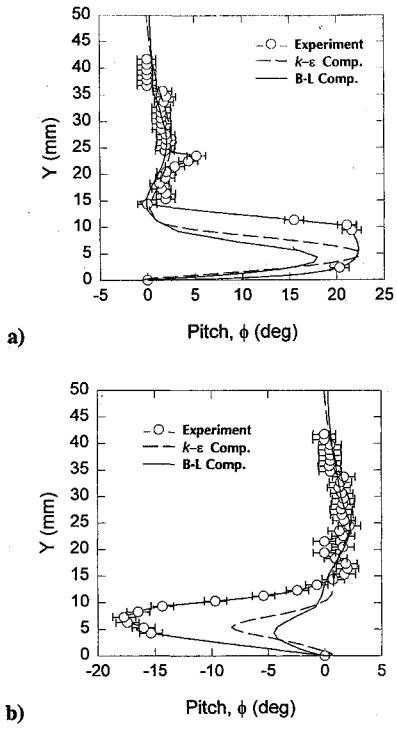

Fig. 13 Comparison of the pitch angle variation in the Y direction at a) $X = 0$ mm and b) $X = 5$ mm.

the flow within this region, including computed particle trajectories, are given in Ref. 9.

Figure 13 compares the computed and experimental pitch angles ϕ for cuts at $X = 0$ and $X = 5$ mm. Along the plane of symmetry, the peak pitch angle within the separated region is accurately predicted by the κ–ε computation and underpredicted by the B–L computation. However, both computations underpredict the vertical extent of the high-pitch region within the separated flow. In the outer flow, both computations match the experimental data.

For the cut along the line $X = 5$ mm, Fig. 13b, the comparison between the experiment and computations is not as good. Within the separated region, both computations significantly underpredict the extent to which the flow is directed downward, toward the plate. This indicates that the computations are most likely not capturing the full details of the mushroom-shaped vortex pattern within the separated region, as shown in Fig. 2. Above the separated region, the computations again accurately represent the experimental data.

A comparison between the computed and experimental yaw angles (not shown) reveals the computations differ significantly from the experiment over the range from $Y = 5$ to 10 mm, with Ψ differences up to 10 deg in this region. Over the rest of the region, the computations are within 2 deg of the experimental results. As with the pitch results, the large errors in yaw angle within the separated region suggest that the computations are not capturing the flow pattern in this area.

Further Comments on the Comparison

Based on the comparison of the flowfield data with the computed solutions presented in the preceding sections, several important conclusions can be made. Within the separated region, distinct differences are apparent between the experiment and computations. From the point of view of understanding the interaction between the outer inviscid flow and the viscous boundary layer, the separated region represents the most important aspect of the crossing-shock interaction. Globally, both computations are able to predict the presence of this region. However, there are significant differences in the values of the flowfield properties predicted within the region. This suggests the computations are not fully capturing all of the physics which govern the interaction.

It is important to understand possible reasons why the computations are in error within the separated region. One likely source of error is in the turbulence models employed. The fluid within the separated region has been shown to be composed of the incoming viscous turbulent boundary layer. Thus, one would expect that the properties in this region would be dependent on the turbulence model. Additionally, it was seen in a previous comparison of the wall skin friction distribution[7] that large errors in the computed wall shear stress occur along the interaction centerline, supporting the argument that the turbulence modeling is in error in this region. Here, both the B–L and κ–ε turbulence models fail in regions of strong gradients, as in two-dimensional compression corner flows with significant separation.

A second possible source of error lies in the resolution of the computations. It was seen in the preceding discussions that the computations smear the shock waves, making it difficult to identify discrete waves. To capture the effects of the plate and fin boundary layers, the computations must have sufficient grid resolution near the model surfaces. However, memory and CPU time constraints then require that the grid resolution must become much coarser away from the surface. The coarse outer grid makes it difficult to precisely capture shocks, resulting in a smearing of the shock waves over a significant distance. This can have a significant impact on the predicted flow directions and property values, especially the static pressure.

Conclusions

Present data obtained through the five-hole probe surveys provide a valuable addition to the overall experimental data set on crossing-shock/boundary-layer interactions. The contour plots complement and validate the previously developed flowfield model of these interactions obtained from planar laser scattering visualizations.[8,9,14] The survey results verify the existence of all of the shock waves identified in the PLS images and provide information on their relative strengths. The surveys also show that the separated region consists of a large, low-Mach-number, low-total-pressure region. Additional understanding of the flow behavior within this region is provided by the pitch and yaw contours, supporting the previously postulated mushroom-shaped vortex pattern.[9] Finally, the experimentally obtained five-hole probe data provide an excellent data set for comparison with computational solutions.

The comparison with the two computed solutions shows that the largest errors in the computed flowfield occur within the separated flow region. Within this region, large errors are observed in the computed static pressure, flow angles, and Mach number. In addition to turbulence model problems, insufficient grid resolution and shock smearing are likely causes of the discrepancies. Outside the separated region, where the flow is essentially inviscid, the computations are in better agreement with the experiment than inside it.

Additionally, the comparison shows that neither computation can be identified as being superior to the other. The same result was observed in comparisons made for a hypersonic interaction at Mach 8.3 (Ref. 21). One explanation is that the possible advantage of the κ–ε turbulence model over the B–L model is obscured by the reduced spatial resolution employed in the κ–ε case. It is important to note that both computations do predict the separation of the incoming boundary layer and the subsequent viscous flow accumulation on the centerline. Within the flowfield, both computations reveal the formation of the low-Mach-number, low-total-pressure region on centerline, providing important overall information on the crossing-shock flow.

Acknowledgments

This work was sponsored by the Air Force Office of Scientific Research under Grants 89-0315 and 86-0266, monitored by Len Sakell, and by NASA Ames Grant NGT-50952, monitored by C. C. Horstman. Supercomputing time was provided by the National Center for Supercomputing Applications by Cray Research Inc. through the 1992 University Research and Development Grant.

References

[1]Mee, D. J., Stalker, R. J., and Stollery, J. L., "Glancing Interactions Between Single and Intersecting Oblique Shock Waves and a Turbulent Boundary Layer," *Journal of Fluid Mechanics*, Vol. 170, Sept. 1986, pp. 411–433.

[2]Batcho, P. F., Ketchum, A. C., Bogdonoff, S. M., and Fernando, E. M., "Preliminary Study of the Interactions Caused by Crossing Shock Waves and a Turbulent Boundary Layer," AIAA Paper 89-0359, Jan. 1989.

[3]Bogdonoff, S. M., and Poddar, K., "An Exploratory Study of a Three-Dimensional Shock Wave Turbulent Boundary Layer Interaction," AIAA Paper 91-0525, Jan. 1991.

[4]Hingst, W. R., and Williams, K. E., "Interaction of Two Glancing, Crossing Shock Waves with Turbulent Boundary Layers at Various Mach Numbers," NASA TM 103740, 1991.

[5]Bogdonoff, S. M., and Stokes, W. L., "Crossing Shock Wave Turbulent Boundary Layer Interactions—Variable Angle and Shock Generator Length Geometry Effects at Mach 3," AIAA Paper 92-0636, Jan. 1992.

[6]Poddar, K., and Bogdonoff, S. M., "A Study of the Unsteadiness of Crossing Shock Wave Turbulent Boundary Layer Interactions," AIAA Paper 90-1456, June 1990.

[7]Garrison, T. J., Settles, G. S., Narayanswami, N., and Knight, D. D., "Laser Interferometer Skin-Friction Measurements of Crossing-Shock Wave/Turbulent Boundary-Layer Interactions," *AIAA Journal*, Vol. 32, No. 6, 1994, pp. 1234–1241.

[8]Garrison, T. J., and Settles, G. S., "Flowfield Visualization of Crossing Shock-Wave/Boundary Layer Interactions," AIAA Paper 92-0750, Jan. 1992.

[9]Garrison, T. J., Settles, G. S., Narayanswami, N., and Knight, D., "Structure of Crossing Shock-Wave/Turbulent Boundary-Layer Interactions," *AIAA Journal*, Vol. 31, No. 12, 1993, pp. 2204–2211.

[10]Garrison, T. J., and Settles, G. S., "Interaction Strength and Model Geometry Effects on the Structure of Crossing-Shock Wave/Turbulent Boundary-Layer Interactions," AIAA Paper 93-0780, Jan. 1993.

[11]Kussoy, M. I., and Horstman, K. C., "Intersecting Shock-Wave /Turbulent Boundary-Layer Interactions at Mach 8.3," NASA TM 103909, Feb. 1992.

[12]Kussoy, M. I., Horstman, K. C., and Horstman, C. C., "Hypersonic Crossing Shock-Wave/Turbulent-Boundary-Layer Interactions," AIAA Paper 93-0781, Jan. 1993.

[13]Forkey, J., Cogne, S., Smits, A., Bogdonoff, S., Lempert, W. R., and Miles, R. B., "Time-Sequenced and Spectrally Filtered Rayliegh Imaging of Shock Wave and Boundary Layer Structure for Inlet Characterization," AIAA Paper 93-2300, June 1993.

[14]Garrison, T. J., "The Interaction Between Crossing-Shock Waves and a Turbulent Boundary Layer," Ph.D. Thesis, Mechanical Engineering Dept., Pennsylvania State Univ., University Park, PA, Aug. 1994.

[15]Davis, D. O., and Hingst, W. R. "Surface and Flow Field Measurements in a Symmetric Crossing Shock Wave/Turbulent Boundary Layer Interaction," AIAA Paper 92-2634, June 1992.

[16]Gaitonde, D., and Knight, D. D., "Numerical Experiments on 3-D Shock Wave-Boundary Layer Interaction Generated by a Sharp Fin," AIAA Paper 88-0309, Jan. 1988.

[17]Reddy, D. R., "3-D Navier–Stokes Analysis of Crossing, Glancing Shocks/Turbulent Boundary Layer Interactions," AIAA Paper 91-1758, June 1991.

[18]Narayanswami, N., Knight, D. D., Bogdonoff, S. M., and Horstman, C. C., "Interaction Between Crossing Oblique Shocks and a Turbulent Boundary Layer," *AIAA Journal*, Vol. 30, No. 8, 1992, pp. 1945–1952.

[19]Narayanswami, N., Knight, D. D., and Horstman, C. C., "The Investigation of a Hypersonic 3-D Crossing Shock/Turbulent Boundary Layer Interaction," *Shock Waves*, Vol. 3, No. 1, 1993, pp. 35–48.

[20]Narayanswami, N., Horstman, C. C., and Knight, D. D., "Numerical Simulation of Crossing Shock/Turbulent Boundary Layer Interaction at Mach 8.3—Comparison of Zero- and Two-Equation Turbulence Models," AIAA Paper 93-0779, Jan. 1993.

[21]Narayanswami, N., Horstman, C. C., and Knight, D. D., "Computation of Crossing Shock/Turbulent Boundary-Layer Interactions at Mach 8.3," *AIAA Journal*, Vol. 31, No. 8, 1993, pp. 1369–1376.

[22]Gaitonde, D., and Shang, J. S., "Calculations on a Double-Fin Turbulent Interaction at High Speed," AIAA Paper 93-3432, Aug. 1993.

[23]Naughton, J., Cattafesta, L., and Settles, G., "A Miniature, Fast Response, 5-Hole Probe for Supersonic Flowfield Measurements," *AIAA Journal*, Vol. 31, No. 3, 1993, pp. 453–458.

[24]Naughton, J. W., "The Enhancement of Compressible Turbulent Mixing Via Streamwise Vorticity," Ph.D. Thesis, Mechanical Engineering Dept., Pennsylvania State Univ., University Park, PA, May 1993.

[25]Rubesin, M., and Rose, W., "The Turbulent Mean Flow Reynolds-Stress and Heat Flux Equations in Mass Averaged Dependent Variables," NASA TMX 62248, March 1973.

[26]Baldwin, B., and Lomax, H., "Thin Layer Approximation and Algebraic Model for Separated Turbulent Flows," AIAA Paper 78-257, Jan. 1978.

[27]Knight, D. D., "A Hybrid Explicit-Implicit Numerical Algorithm for the Three Dimensional Compressible Navier–Stokes Equations," *AIAA Journal*, Vol. 22, No. 8, 1984, pp. 1056–1061.

[28]Rodi, W., "Experience with Two-Layer Models Combining the k–ε with a One-Equation Model Near the Wall," AIAA Paper 91-0216, Jan. 1991.

[29]MacCormack, R. W., "A Numerical Method for Solving the Equations of Compressible Viscous Flow," *AIAA Journal*, Vol. 20, No. 9, 1982, pp. 1275–1281.

[30]Knight, D. D., Horstman, C. C., Shapey, B., and Bogdonoff, S. M., "Structure of Supersonic Flow Past a Sharp Fin," *AIAA Journal*, Vol. 25, No. 10, 1987, pp. 1331–1337.